Improved precision at high-spatial resolution of strontium isotope analysis in apatite and apatite inclusions by LA-MC-ICP-MS with 1013 Ω amplifiers

Anda Buzenchi, Hugo Moreira, Emilie Bruand, Olivier Bruguier, Bruno Dhuime

Chemical Geology 666 (2024) 122306

Contents lists available at ScienceDirect

Chemical Geology

journal homepage: www.elsevier.com/locate/chemgeo

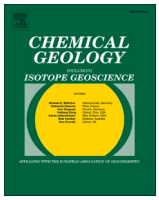

Improved precision at high-spatial resolution of strontium isotope analysis in apatite and apatite inclusions by LA-MC-ICP-MS with 10^{13} Ω amplifiers

Anda Buzenchi [a,*], Hugo Moreira [a], Emilie Bruand [b], Olivier Bruguier [a], Bruno Dhuime [a]

[a] CNRS-UMR5243, Géosciences Montpellier, Université de Montpellier, 34095, Montpellier Cedex 05, France
[b] Laboratoire Geo-Ocean, CNRS, Université de Bretagne Occidentale, France

ARTICLE INFO

Editor: Dr. S Aulbach

Keywords:
Sr isotopes
Apatite
Mineral inclusions
10^{13} Ω amplifiers
LA-MC-ICP-MS

ABSTRACT

Recent advancements in in situ analytical techniques have generated new interest in measuring strontium (Sr) isotopes in rock-forming apatite and apatite inclusions in zircon, because they can bring new insights into the primary signatures of magmatic sources. This paper introduces a novel approach based on laser ablation multi-collector inductively coupled plasma mass spectrometry (LA-MC-ICP-MS), which allows to achieve higher precision in situ analysis of Sr isotopes in small volumes of samples. The use of 10^{13} Ω current amplifiers for the acquisition of the signal on *m/z* 83, 83.5, 84, 85, 85.5, 86, 86.5, 87 and 88, along with a specific data reduction protocol, enhance both the internal precision and the external reproducibility of the $^{87}Sr/^{86}Sr$ ratio by a factor of four, presenting a significant improvement over the conventional use of 10^{11} Ω amplifiers. An internal precision better than 0.45‰ (i.e. 450 ppm; 2 s.e.) on the $^{87}Sr/^{86}Sr$ ratio can be achieved on the Durango apatite standard with a 13 μm square-shaped laser beam and a laser ablation pit of 60 μm depth. With a 5 μm beam, the precision is 2.2‰ on average with a 10 μm ablation pit depth for this standard. This analytical procedure was applied to investigate Sr isotopes in apatite and apatite inclusions within zircons from seven high Ba—Sr magmatic rocks in the Northern Highland Terrane, Scotland. For these well-characterised, geochemically undisturbed samples, the data reveals similar Sr isotope compositions between apatite inclusions armoured in zircon, matrix apatites, and the bulk rock. This highlights the ability of apatite inclusions to faithfully record primary signatures of host magmas, elucidating their utility as reliable indicators in petrological studies of ancient samples.

1. Introduction

The Sr isotope investigation of apatite ($(Ca_5PO_4)_3(OH, Cl, F)$) has received increasing interest over the last years with the recent development of in situ analyses (Buzenchi et al., 2023; Caton et al., 2022; Emo et al., 2018; Gillespie et al., 2021a, 2021b; Horstwood et al., 2008; Müller and Anczkiewicz, 2016; Ravindran et al., 2020; Yang et al., 2014a). Apatite is an accessory mineral ubiquitous in igneous rocks, and it can be found as inclusions in magmatic silicate minerals such as zircon and titanite (Bruand et al., 2016). It is largely used for Sr isotope studies because it does not incorporate Rb, and therefore accounts for negligible ingrowth of radiogenic ^{87}Sr from ^{87}Rb beta decay. This allows a good estimation of the initial $^{87}Sr/^{86}Sr$ ratio of the magmatic sources, assuming that primary signatures are preserved in apatite. One of the main advantages of studying apatite inclusions is that inclusions are protected by their host mineral, which limits the degree to which the measured $^{87}Sr/^{86}Sr$ ratio may be shifted from its initial value during secondary (i.e. post-crystallisation) processes (Caton et al., 2022; Emo et al., 2018; Ravindran et al., 2020). Robust hosts minerals, such as zircon, can provide temporal context from U—Pb dating, along with geochemical context from the analysis of Hf isotopes, O isotopes and trace elements (Dhuime et al., 2012; Kemp et al., 2010; Valley et al., 1998). When combined with Sr isotopes in apatite inclusions, the information preserved in zircon constitutes a unique and powerful tool to provide further constraints in petrological studies, and to track changes in the composition of the continental crust though time (Dhuime et al., 2014; Gillespie et al., 2021a; Ravindran et al., 2020).

Recent developments in both LA-MC-ICP-MS (Buzenchi et al., 2023; Emo et al., 2018) and secondary ionisation mass spectrometry (SIMS) (Gillespie et al., 2021b) allow to measure $^{87}Sr/^{86}Sr$ ratios in apatite with an internal precision (given by 2 × standard error of *n* cycles integrated in a measurement; or 2 s.e.) better than 3‰ for analytical beam sizes of 15–10 μm in diameter. However, an inherent challenge of investigating apatite inclusions in zircon consists in developing new ways to measure

* Corresponding author.
E-mail address: anda-ioana.buzenchi@umontpellier.fr (A. Buzenchi).

https://doi.org/10.1016/j.chemgeo.2024.122306
Received 26 April 2024; Received in revised form 30 July 2024; Accepted 31 July 2024
Available online 4 August 2024

Table 1
MC-ICP-MS (Neptune XT) cup configuration and potential isobaric interferences.

Faraday cup	L4	L3	L2	L1	C	H1	H2	H3	H4
Amplifier (Ω)	10^{13}	10^{13}	10^{13}	10^{13}	10^{13}	10^{13}	10^{13}	10^{13}	10^{13}
m/z	83	83.5	84	85	85.5	86	86.5	87	88
Sr			$^{84}Sr^{+}$			$^{86}Sr^{+}$		$^{87}Sr^{+}$	$^{88}Sr^{+}$
Rb				$^{85}Rb^{+}$				$^{87}Rb^{+}$	
Kr	$^{83}Kr^{+}$		$^{84}Kr^{+}$			$^{86}Kr^{+}$			
Er	$^{166}Er^{++}$	$^{167}Er^{++}$	$^{168}Er^{++}$	$^{170}Er^{++}$					
Yb			$^{168}Yb^{++}$	$^{170}Yb^{++}$	$^{171}Yb^{++}$	$^{172}Yb^{++}$	$^{173}Yb^{++}$	$^{174}Yb^{++}$	$^{176}Yb^{++}$
Lu									$^{176}Lu^{++}$
Hf									$^{176}Hf^{++}$
Ca dimers	$^{40}Ca^{43}Ca^{+}$		$^{42}Ca^{42}Ca^{+}$ $^{40}Ca^{44}Ca^{+}$			$^{42}Ca^{44}Ca^{+}$ $^{40}Ca^{46}Ca^{+}$ $^{43}Ca^{43}Ca^{+}$		$^{43}Ca^{44}Ca^{+}$	$^{40}Ca^{48}Ca^{+}$ $^{44}Ca^{44}Ca^{+}$ $^{42}Ca^{46}Ca^{+}$
Ca argides	$^{43}Ca^{40}Ar^{+}$		$^{44}Ca^{40}Ar^{+}$ $^{46}Ca^{38}Ar^{+}$ $^{48}Ca^{36}Ar^{+}$			$^{46}Ca^{40}Ar^{+}$ $^{48}Ca^{38}Ar^{+}$			$^{48}Ca^{40}Ar^{+}$

Table 2
Typical operating conditions for LA-MC-ICP-MS analyses.

Neptune XT MC-ICP-MS	
Extraction voltage	−2000
Focus voltage	−609
Cool gas (l/min)	15.1
Auxiliary gas (l/min)	0.8
Sample gas (l/min)	1
Analyte Excite +	
MFC1 He (l/min)	0.35
MFC2 He (l/min)	0.17
MFC3 N_2 (ml/min)	10
Repetition rate (Hz)	4 to 5
Fluence (J/cm2)	6
Maximum depth of laser ablation (μm)	60
Square-shaped beam size (length x width) for standards (μm)	13 × 13,10 × 10, 7 × 7, 5 × 5
Square-shaped beam size (length x width) for matrix apatites (μm)	9 × 9, 11 × 11,12 × 12,13 × 13
Rectangular-shaped beam size for apatite inclusions	best fit to inclusion size and shape

smaller volumes of material, since a large majority of inclusions are very small in size and require a spatial resolution better than 15–10 μm.

Analyses of small volumes of material can produce low ion beam currents (typically <1e10^{-13} A), and their measurement is perturbated by low signal-to-noise ratios (S/N). MC-ICP-MS instruments are usually equipped with Faraday cups connected to 10^{11} Ω amplifiers, which produce a relatively high instrumental noise of ~4e10^{-16} A. As a consequence, the signal measured when ablating small sample volumes may be below the limit of detection (LOD) of the instrument, and even if it is above the LOD, a small signal intensity will limit the efficiency of mass bias and interference corrections, and ultimately produces large uncertainties over the determination the final isotope ratios. One approach to obtain highly precise isotope ratios at low intensities is to improve the S/N ratio through the use of amplifiers with higher ohmic resistors, such as 10^{13} Ω (Koornneef et al., 2014). This approach has been extensively developed for MC-ICP-MS (Creech et al., 2020; Makishima and Nakamura, 2010, 2012; Schulz et al., 2013), and more recently for LA-MC-ICP-MS (Craig et al., 2017; Kimura et al., 2016; Lloyd et al., 2018; Yamamoto et al., 2021). Overall, these studies have proven that higher precision measurements can be obtained with 10^{13} Ω amplifiers, which are highly stable and linear over a wide dynamic range of ion beam intensities and produce lower instrumental noise of ~4e10^{-18} A. In a recent study, we have proposed a new approach to improve both the precision and the accuracy of $^{87}Sr/^{86}Sr$ ratios measured by LA-MC-ICP-MS with 10^{11} Ω amplifiers (Buzenchi et al., 2023), and the potential of 10^{13} Ω amplifiers with this approach yet has to be demonstrated.

Here we present LA-MC-ICP-MS Sr isotope data for a selection of five apatite standards analysed with square-shaped laser beams ranging from 13 μm to 5 μm in size. The comparison between data obtained with 10^{11} Ω and 10^{13} Ω amplifiers on the Durango apatite reference material highlights the potential of 10^{13} Ω amplifiers to better unpick low intensity beams and correct for isobaric interferences. For this standard, an average precision of 1.5 ‰ was obtained at a spatial resolution of (length x width x depth) 5x5x60 μm, and a precision of 2.2‰ can be achieved at a high-spatial resolution of 5x5x10 μm. This new approach is especially well suited for studying apatite inclusions in zircon.

We further present Sr isotope analyses of matrix apatite and apatite inclusions in zircon from seven high Ba—Sr magmatic rocks from the Strontian and Rogart plutons (Northern Highland Terrane, Scotland). These samples have been extensively studied over the last 20 years (Fowler et al., 2001; Fowler and Rollinson, 2012), and they have presumably not been affected by secondary processes (e.g., alteration, metamorphism) that could overprint their original chemical signature. (Bruand et al., 2014, 2016, 2017, 2019, 2020, 2023; Fowler et al., 2001, 2008). Our data show that the Sr isotope composition of apatite inclusions in zircon is similar to that of matrix apatites and the bulk rock of a given sample, demonstrating the potential of the apatite inclusions record in ancient magmatic rocks where metamorphism is pervasive.

2. Analytical conditions and data reduction

All analyses were performed at the MILESTONE laboratory (Géosciences Montpellier), which is part of the ISOTOP-MTP platform of the RéGEF (https://www.regef.fr/). It hosts a Thermo Scientific Neptune XT MC-ICP-MS equipped with an Edwards nXL110i dry interface pump, along with 'jet' sample and 'X' skimmer cones. The Faraday cup configuration and typical operating conditions are detailed in Table 1 and Table 2, respectively.

The MC-ICP-MS was coupled with a Teledyne Cetac Analyte Excite+ excimer laser equipped with an optional X-Y Theta dynamic aperture allowing rectangular-shaped laser beams of any aspect ratio (length x width) and orientation to be generated. The HelEx II 2-volumes ablation cell is equipped with the Aerosol Rapid Introduction System (ARIS), which enhances particle transport, reduces oxides formation and improves sensitivity (Craig et al., 2018). Tuning for maximum sensitivity, signal stability and best peak shape was performed daily in rastering ablation mode (along ca. 1 mm lines) using Durango apatite with a square-shaped 13 μm laser ablation beam, a fluence of 6 J/cm^2, a 6 Hz repetition rate and a 5 μm/s scan speed. Typical intensity on $^{88}Sr^{+}$ with these conditions was approximately 0.25 V and UO^{+}/U^{+} was <0.1%. Sr isotope ratios were measured during 60 cycles of 1 s each. Before each

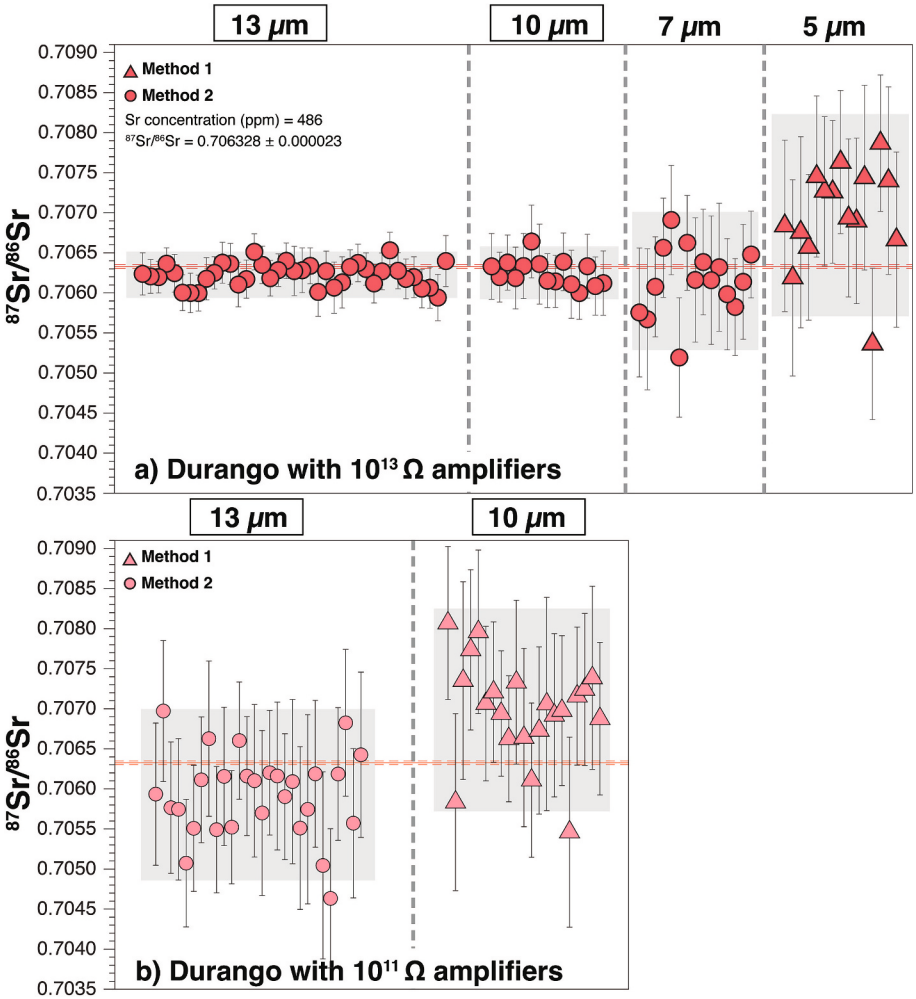

Fig. 1. Compilation of $^{87}Sr/^{86}Sr$ ratios obtained by LA-MC-ICP-MS on the Durango apatite a) with 10^{13} Ω amplifiers and with square-shaped laser beams ranging from 13 µm to 5 µm in size; and b) with 10^{11} Ω amplifiers and square-shaped laser beams of 13 µm and 10 µm (Buzenchi et al., 2023). Error bars are 2 s.e. Grey fields are the 2 s.d. of repeated measurements at a given beam size. Solid and dashed red lines are the Yang et al. (2014b) reference value and the 2 s.d., respectively, for this standard. (0.706328 ± 0.000023). (For interpretation of the references to colour in this figure legend, the reader is referred to the web version of this article.)

measurement, an on-peak gas line wash-out of 40 cycles of 1 s, and a gas blank of 120 cycles of 1 s, were performed.

The MILESTONE Neptune XT MC-ICP-MS is equipped with nine 10^{13} Ω amplifiers (Table 1). The use of 10^{13} Ω amplifier technology was first described by Koornneef et al. (2014), who showed that these resistors perform better than ion counting and 10^{11} Ω amplifiers when measuring Sr and Nd isotopes by TIMS. Compared to 10^{11} Ω amplifiers, 10^{13} Ω amplifiers have an improved signal-to-noise ratio by 4 to 5 fold (Craig et al., 2019), which contributes to a similar improvement in the precision of small ion beam analyses. Importantly, 10^{13} Ω amplifiers experience a time offset and a slower signal decay compared to 10^{11} Ω amplifiers. The difference in the signal response can bias the accuracy of the results (Pettke et al., 2011), and therefore a 'tau' (τ) correction needs to be applied. The τ correction uses an exponential offset equation to calculate the true signal intensity, using the measured intensity and a τ decay constant that is calculated for each amplifier after installation and is assumed to remain constant (Craig et al., 2019; Kimura et al., 2016). The tau-corrected ion signal $I_{corr}(t_i)$ at the time t_i is calculated with eq. (1) below:

$$I_{corr(t_i)} = I_{m(t_i)} + \frac{I_{m(t_{i+1})} - I_{m(t_{i-1})}}{t_{(i+1)} - t_{(i-1)}} x\,\tau \quad (1)$$

with $I_m(t_i)$, $I_m(t_{i+1})$ and $I_m(t_{i-1})$ the measured intensities of each isotope at times t_i, t_{i+1}, and t_{i-1}, respectively; and τ the tau-correction factor of the amplifier that is considered.

The stability of the ion beam is an important factor when using 10^{13} Ω amplifiers, and successful analyses with no correction of the slow response and decay have been reported for TIMS analyses at stable ion beams (Klaver et al., 2016). MC-ICP-MS analyses in solution mode usually require a τ correction (Craig et al., 2017; Lloyd et al., 2018). Comparatively, when MC-ICP-MS is combined with a laser ablation system, the ion beams produced are much less stable than those produced by TIMS and solution MC-ICP-MS techniques. This instability is essentially caused by the size of particles ablated, the way particles are transported from the sample to the plasma by the carrier gas flow, downhole fractionation, etc. As a consequence, transient signals inherent to the LA-MC-ICP-MS technique systematically require a τ correction to achieve highly precise/accurate data (Craig et al., 2019).

The raw data intensities were reduced offline using an in-house Excel spreadsheet. For each *m/z* of interest, the gas blank intensities were filtered using a 2 x standard deviation (2 s.d.) rejection threshold for individual cycles, and the mean intensity of the background was subtracted from the raw intensity of the sample measured. Krypton was assumed to be only present in the gas and the contribution of Kr on *m/z* 83, 84 and 86 was considered negligible after background correction. For interferences and mass bias corrections, we used the data reduction scheme recently developed by Buzenchi et al. (2023) for the analysis of small volumes of apatite by LA-MC-ICP-MS. Exponential mass bias

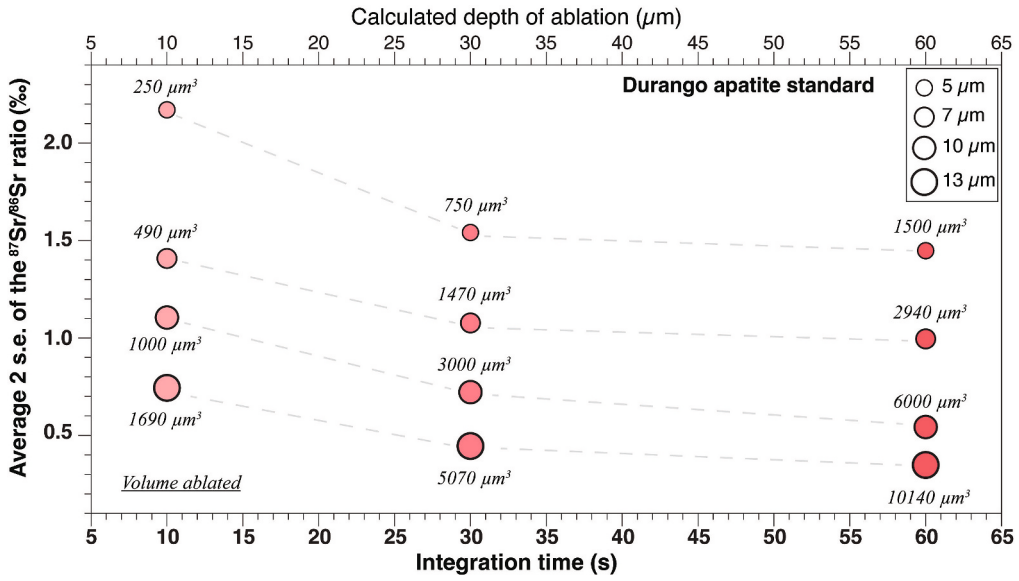

Fig. 2. Average precision of the $^{87}Sr/^{86}Sr$ ratio in Durango apatite with 13 μm, 10 μm, 7 μm and 5 μm laser ablation beams, as a function of the integration time of the ion beam signal for individual measurements (10s, 30s or 60 s). The depth of ablation was estimated from the measurement of laser pits after 60s ablation (see supplementary material).

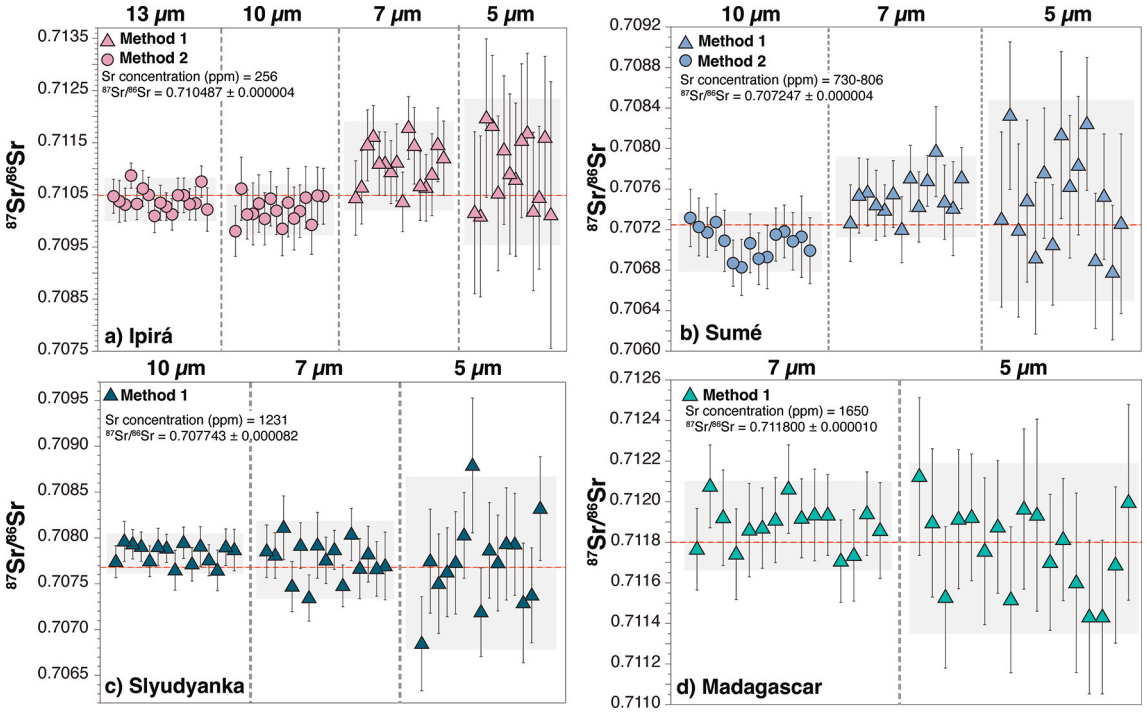

Fig. 3. Compilation of $^{87}Sr/^{86}Sr$ ratios obtained by LA-MC-ICP-MS on a) Ipirá, b) Sumé, c) Slyudyanka and d) Madagascar apatites, with square-shaped laser beams ranging between 13 μm and 5 μm in size. See caption of Fig. 1 for details. The red line in a) and b) is the solution MC-ICP-MS value of Buzenchi et al. (2023). The red line in c) and d) is the reference value of Yang et al. (2014b). (For interpretation of the references to colour in this figure legend, the reader is referred to the web version of this article.)

correction was applied by using the βSr value calculated from the measured $^{88}Sr/^{86}Sr$ and $^{88}Sr/^{86}Sr_{(natural)} = 8.375209$ (Thirlwall, 1991). When $^{173}Yb^{++}$ was measured below the global limit of detection (defined as LOD_{global} = 3 s.d. of the means of all gas blanks measured during the session), the *Method 1* of Buzenchi et al. (2023), which only corrects measured intensities for gas blank and instrumental mass bias, was selected. When $^{173}Yb^{++}$ was measured above LOD_{global}, we used the *Method 2* of Buzenchi et al. (2023), which additionally corrects for isobaric interferences of doubly-charged Yb and Er, ^{87}Rb, and Ca dimers.

3. Analysis of apatite standards with 10^{13} Ω amplifiers

3.1. Methodology

Five apatite standards, Durango (Thomson et al., 2012; Yang et al., 2014b); Ipirá (Alba et al., 1983; Buzenchi et al., 2023); Sumé (Lana et al., 2022); Madagascar (Thomson et al., 2012; Yang et al., 2014b); and Slyudyanka (Chew et al., 2011; Yang et al., 2014b), with a wide range of ages (32.7 Ma to 2 Ga) and Sr and REE concentrations (Sr = 250–1650

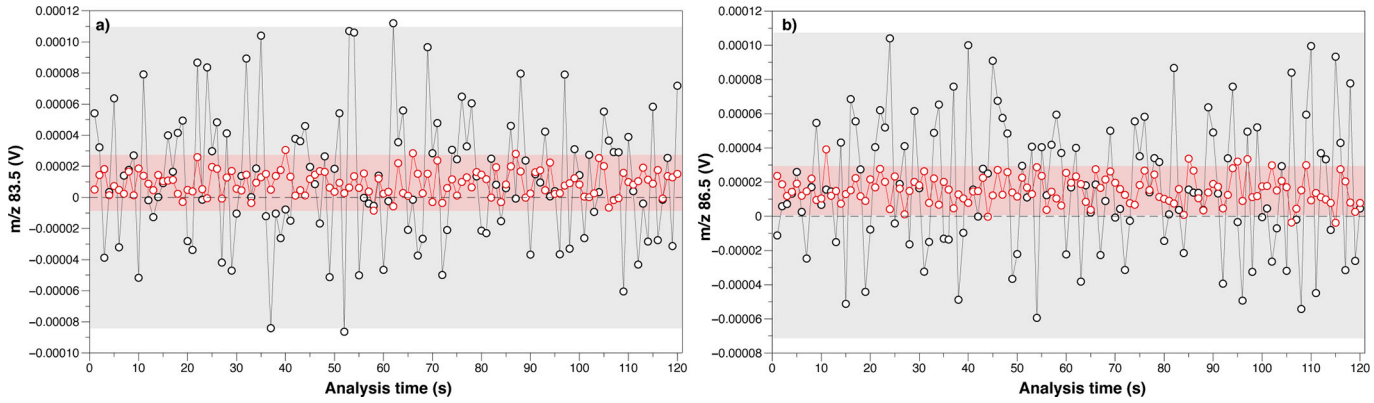

Fig. 4. Gas background intensities measured during 120 s with a 10^{11} Ω amplifier (grey data) and a 10^{13} Ω amplifier (red data) configuration for a) *m/z* 83.5 and b) *m/z* 86.5. Grey and red horizontal fields represent the 3 s.d. of the 10^{11} Ω and 10^{13} Ω data, respectively. (For interpretation of the references to colour in this figure legend, the reader is referred to the web version of this article.)

ppm; Er = 2–83 ppm; Yb = 4–60 ppm), were selected. All standards were ablated using 5 μm and 7 μm square-shaped laser beams. Slyudyanka, Durango and Ipirá were also analysed at 10 μm, and only Durango and Ipirá were analysed at 13 μm. An SEM image of ablation pits produced at different laser beam sizes is provided in the Supplementary material. We note that higher spot sizes could only be achieved in standards with lower Sr contents, when the $^{88}Sr^{+}$ beam did not exceed the 5000 fA limit that can be measured with 10^{13} Ω resistors.

3.2. Precision, accuracy and reproducibility of $^{87}Sr/^{86}Sr$ ratios

A summary of 85 analyses of the Durango apatite is presented in Fig. 1a. At 13 μm, the internal precision of individual $^{87}Sr/^{86}Sr$ measurements (given by the 2 s.e. of the mean of 60 cycles integrated) is better than 0.45‰, and repeated measurements give an average $^{87}Sr/^{86}Sr$ of 0.706226 ± 0.000288 (2 s.d.; n = 39). At 10 μm the internal precision is <0.50‰, and it is <0.87‰ ppm at 7 μm and < 1.7‰ at 5 μm. Average $^{87}Sr/^{86}Sr$ ratios obtained from repeated measurements at 10 μm, 7 μm and 5 μm all overlap within error (10 μm: 0.706250 ± 0.000338 (n = 15); 7 μm: 0.706149 ± 0.000863 (n = 15); 5 μm: 0.706969 ± 0.001262 (n = 15)). Overall, the average $^{87}Sr/^{86}Sr$ ratios obtained at four laser ablation beam sizes are within error the Yang et al. (2014b) reference value for this standard (0.706328 ± 0.000023; 2 s.d.), and within error of the solution MC-ICP-MS (0.706320 ± 0.000005) and LA-MC-ICP-MS (0.706392 ± 0.000163) average values recently published by Buzenchi et al. (2023). A summary of 49 analyses of the Durango apatite at 13 μm and 10 μm measured using 10^{11} Ω resistors from Buzenchi et al. (2023), is presented in Fig. 1b. This allows a direct comparison of Sr isotope data for similar volumes of material ablated when using two different types of amplifiers. This aspect is further discussed in Section 3.3.

The relationship between the volume of Durango apatite ablated and the precision of the $^{87}Sr/^{86}Sr$ ratio measured with 10^{11} Ω amplifiers is illustrated in Fig. 2. Volumes were calculated from the dimensions (length x width) of the laser ablation beams and the depth of ablation pits measured after 60s of ablation. Perhaps unsurprisingly, the precision becomes lower at high spatial resolution, but it is striking that a good precision 2.2 ‰ can be reached at 5x5x10 μm, i.e. for an ablated volume of only 250 μm^3. An ablated volume six times larger is required to improve the precision to 1.5 ‰ at 5x5x60 μm.

Sixty-three analyses of the Ipirá apatite are presented in Fig. 3a. The internal precision of individual $^{87}Sr/^{86}Sr$ measurements is better than 0.59‰ with 13 μm laser ablation beams, and repeated measurements give an average $^{87}Sr/^{86}Sr$ of 0.710409 ± 0.000414 (2 s.d.; n = 17). At 10 μm the internal precision is <0.92‰, and it is <1.1‰ at 7 μm and < 2.2‰ at 5 μm. Average $^{87}Sr/^{86}Sr$ ratios obtained from repeated measurements at 10 μm, 7 μm and 5 μm all overlap within error (10 μm: 0.710215 ± 0.000489 (n = 16); 7 μm: 0.711053 ± 0.000854 (n = 16); 5 μm: 0.710940 ± 0.001403 (n = 14)). Overall, the average $^{87}Sr/^{86}Sr$ obtained using four laser beam sizes are within error of the solution MC-ICP-MS (0.710487 ± 0.000004; 2 s.d.) and LA-MC-ICP-MS (0.710542 ± 0.000147) average values of Buzenchi et al. (2023).

A compilation of 45 analyses of the Sumé apatite is presented in Fig. 3b. At 10 μm, the internal precision of the $^{87}Sr/^{86}Sr$ ratio is better than 0.57‰, and repeated measurements give an average $^{87}Sr/^{86}Sr$ of 0.707081 ± 0.0002296 (2 s.d.; n = 15). At 7 μm the internal precision is <0.65‰, and it is <1.2‰ at 5 μm. Average $^{87}Sr/^{86}Sr$ obtained from repeated measurements at 7 μm and 5 μm all overlap within error (7 μm: 0.707522 ± 0.000399 (n = 14); 5 μm: 0.707487 ± 0.000993 (n = 15)). All data are within error of the solution MC-ICP-MS (0.707247 ± 0.000004; 2 s.d.) and LA-MC-ICP-MS (0.707266 ± 0.000139) average values of Buzenchi et al. (2023).

Forty-five analyses of the Slyudyanka apatite are reported in Fig. 3c. The internal precision of the $^{87}Sr/^{86}Sr$ ratio is better than 0.32‰, 0.52‰ and 1.0‰ at 10 μm, 7 μm and 5 μm, respectively. Average $^{87}Sr/^{86}Sr$ obtained from repeated measurements at different spot sizes all overlap within error (10 μm: 0.707830 ± 0.000220 (2 s.d.; n = 15); 7 μm: 0.707760 ± 0.000427 (n = 15); 5 μm: 0.707726 ± 0.000943 (n = 12)). These data are within error the Yang et al. (2014b) reference value for this standard (0.707690 ± 0.000015; 2 s.d.), and also within error of the solution MC-ICP-MS (0.707705 ± 0.000004) and the LA-MC-ICP-MS (0.707743 ± 0.000082) values of Buzenchi et al. (2023).

A summary of 32 analyses of the Madagascar apatite is plotted in Fig. 3d. At 7 μm and 5 μm, the internal precision of the $^{87}Sr/^{86}Sr$ ratio is better than 0.33‰ and 0.52‰, respectively. Average $^{87}Sr/^{86}Sr$ ratios obtained from repeated measurements are 0.711882 ± 0.000220 (2 s.d.; n = 15) at 7 μm, and 0.711770 ± 0.000420 (n = 17) at 5 μm. This is consistent with the reference value of Yang et al. (2014b) (0.711800 ± 0.000010; 2 s.d.), and solution MC-ICP-MS (0.711814 ± 0.000003) and LA-MC-ICP-MS (0.711821 ± 0.000063) values of Buzenchi et al. (2023).

3.3. Comparison between 10^{13} Ω and 10^{11} Ω amplifiers data

The precision of analyses is limited by the electrical Johnson-Noise of the feedback resistors of the Faraday cups. Improving the S/N of the detectors therefore has potential to enhance the precision of measurements at small intensity beams.

The Johnson-Nyquist noise (JN) is defined as $JN = \sqrt{4 \times k_B \times R \times Tk/Ts}$, where JN is the Johnson-Noise in Volt, k_B is the Boltzman constant ($k_B = 1.380649 \times 10^{-23}$ J.K^{-1}), R is the resistor value in Ω, Tk is the temperature in Kelvin and Ts is the integration time in seconds. Assuming that Tk and Ts remain unchanged, the signal/Johnson-Noise ratio improves with the square root of the resistor value (R). A 10^{13} Ω resistor therefore has a S/N ratio 10 times better than a 10^{11} Ω resistor at

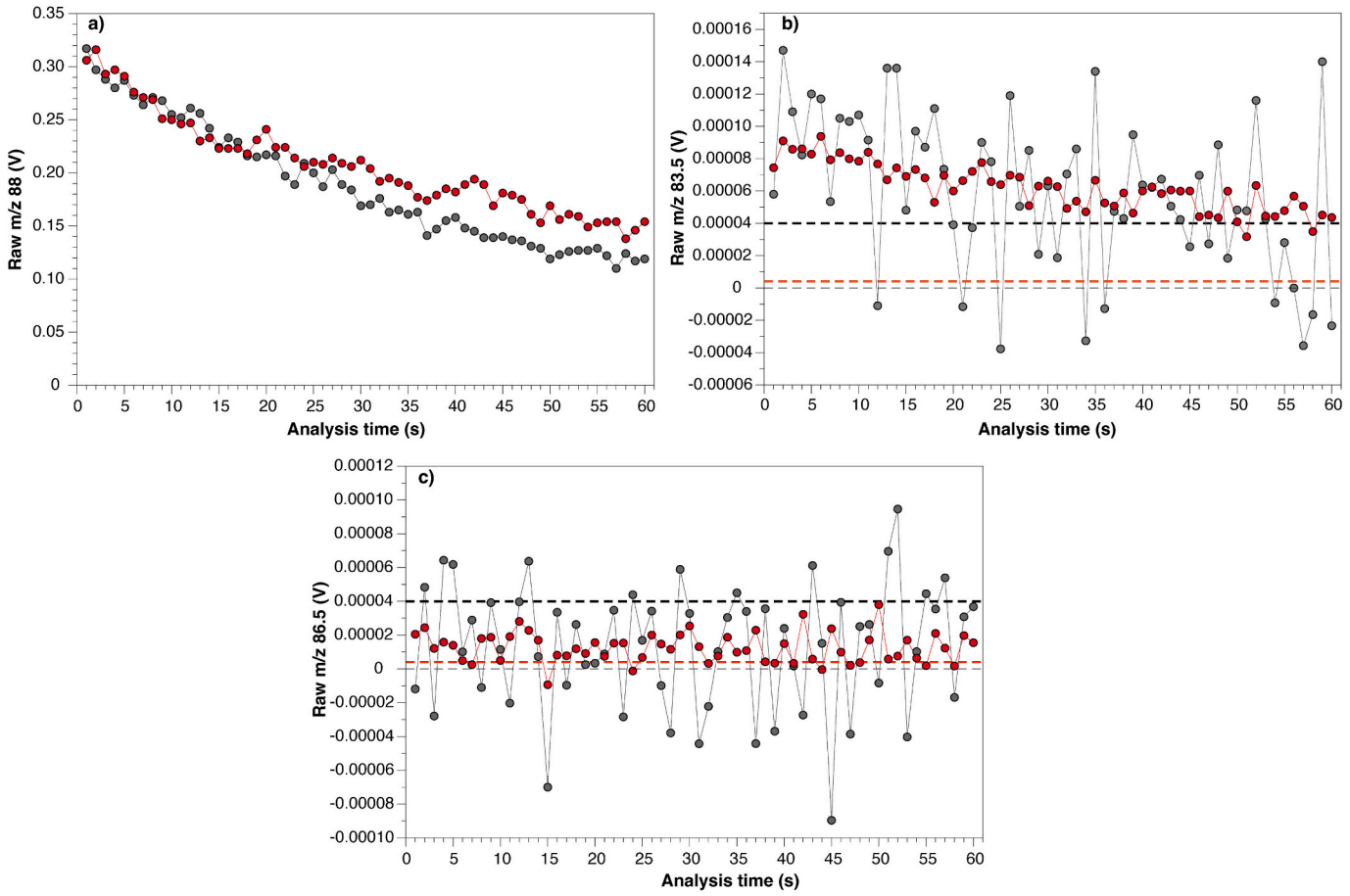

Fig. 5. Intensities measured on *m/z* 88, 83.5 and 86.5 while ablating the Durango apatite (13 μm laser beam). Grey and red symbols are data measured with 10^{11} Ω and 10^{13} Ω amplifiers, respectively. Black and red horizontal dashed lines in panels b) and c) are the Johnson-Noise values for 10^{11} Ω and 10^{13} Ω amplifiers, respectively. 10^{11} Ω amplifiers data from Buzenchi et al. (2023).

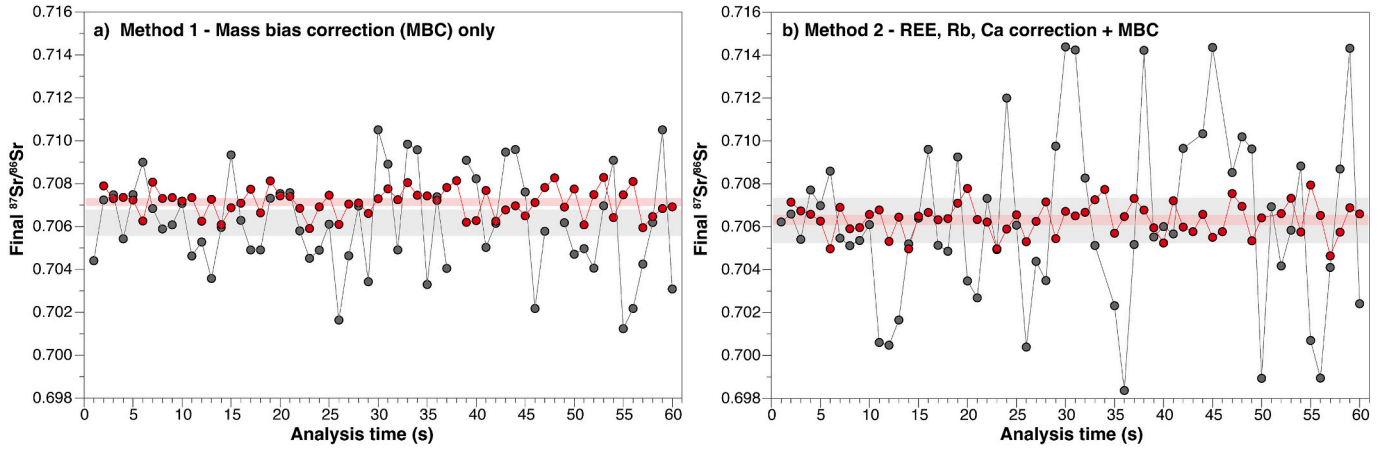

Fig. 6. Evolution of $^{87}Sr/^{86}Sr$ ratios during ablation of the Durango apatite (13 μm laser beam). Symbols colours are same as in Fig. 5. The two approaches of Buzenchi et al. (2023) were used for data reduction after subtraction of the gas blank: a) *Method 1* that only corrects for mass bias after background removal; and b) *Method 2* that also corrects for REE, Rb and Ca interferences on Sr isotopes. Pink and grey fields represent the 2 s.e. of the measurements. 10^{11} Ω amplifiers data from Buzenchi et al. (2023). (For interpretation of the references to colour in this figure legend, the reader is referred to the web version of this article.)

a given intensity, with respect to the Johnson-Noise (Wieser and Schwieters, 2005). In other words, by increasing the resistor value from 10^{11} to 10^{13} Ω (i.e., by a factor of 100), the increase in noise is $\sqrt{100}$, which implies an overall improvement of 10 times in the S/N ratio. This improvement in S/N however has a downside, as higher resistor amplifiers have a lower upper dynamic range. For instance, the upper dynamic range of a 10^{11} Ω amplifier is 500,000 fA (i.e. 50 V), versus 5000 fA (i.e. 0.5 V equivalent on a 10^{11} Ω amplifier) for a 10^{13} Ω amplifier. The contribution of the JN to the internal precision of the analyses is calculated with the eq. (2) below:

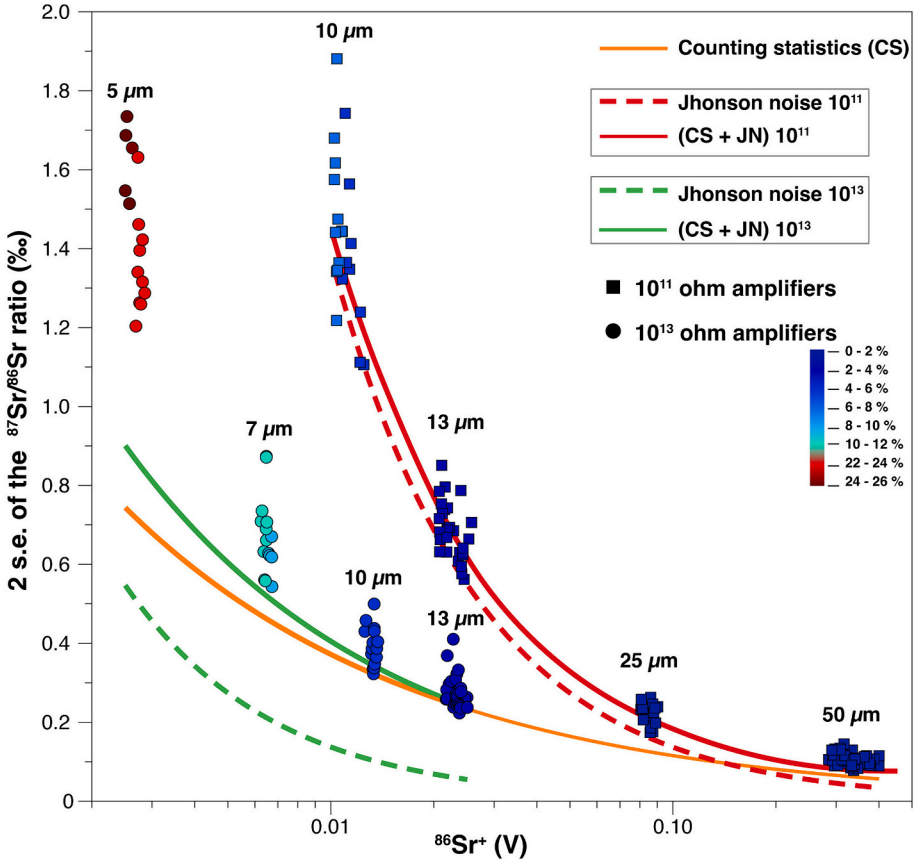

Fig. 7. Internal precision (given by the 2 s.e. of the $^{87}Sr/^{86}Sr$ ratio) of the LA-MC-ICP-MS data as a function of the $^{86}Sr^{+}$ intensity measured on the Durango apatite, with 10^{11} Ω (squares) and 10^{13} Ω (circles) amplifiers. The solid orange curve represents the theoretical precision given by counting statistics (CS). Dashed red and dashed green curves represent the contribution of Johnson-Nyquist noise (JN) to the internal precision. The solid red and solid green curves represent the sum of the contributions of the CS and JN. 10^{11} Ω data are from Buzenchi et al. (2023). The dark blue to dark red colour gradient that is used for data points indicates the proportion of gas blank intensity in the total intensity measured during ablation, from 0% (dark blue) to 26% (dark red). (For interpretation of the references to colour in this figure legend, the reader is referred to the web version of this article.)

$$2\,\text{s.e.}_{(JN)} = 2 \times \frac{\left(\frac{^{87}Sr_{(V)}}{^{86}Sr_{(V)}}\right) \times \sqrt{\left[\left(\frac{0.000042}{^{87}Sr_{(V)}}\right)^2 + \left(\frac{0.000042}{^{86}Sr_{(V)}}\right)^2\right]}}{\sqrt{\text{no.cycles}}} \quad (2)$$

In apatite, isobaric interferences measured on Sr masses have very low intensities (e.g., ~0.05 mV on *m/z* 83.5 and ~ 0.01 mV on *m/z* 86.5 for Durango at 13 μm), and the correction of Er and Yb interferences on Sr isotopes is key to achieve precise and accurate Sr isotope ratios (Buzenchi et al., 2023; Lugli et al., 2020; Ramos et al., 2004; Yang et al., 2014a). The Fig. 4 shows an example of gas background measurements on *m/z* 83.5 ($^{167}Er^{++}$) and 86.5 ($^{173}Yb^{++}$) with two different amplifier configurations, i.e. when using 10^{11} Ω or 10^{13} Ω resistors. A lower amplitude of the signal is observed with the 10^{13} Ω amplifier, which is direct evidence of its lower Johnson-Noise than the 10^{11} Ω amplifier. The limit of detection, which is given by the 3 s.d. of the 120 cycles integrated in Fig. 4a and b, is 0.015 mV for the 10^{13} Ω amplifier, versus 0.11 mV for the 10^{11} Ω amplifier, which represents a 7-fold improvement.

Typical intensities measured on *m/z* 83.5 and 86.5 while ablating Durango apatite with a 13 μm laser ablation beam are summarised in Fig. 5. The $^{87}Sr/^{86}Sr$ ratios obtained with the *Method 1* and *Method 2* approaches of Buzenchi et al. (2023) for data reduction are presented in Fig. 6. Intensities measured with 10^{13} Ω amplifiers are clearly less scattered and better distinguished from the Johnson-Noise than with 10^{11} Ω amplifiers (Fig. 5). Finally, the internal precision (2 s.e.) of the $^{87}Sr/^{86}Sr$ ratio is improved by a factor of 3–5 when using 10^{13} Ω amplifiers (Fig. 6).

Counting statistics (CS) sets a theoretical limit on the analytical precision that can be achieved for a given number of ions counted (John and Adkins, 2010). The contribution of the CS to the internal precision of the analyses is calculated with the eq. (3) below:

$$2\,\text{s.e}_{(CS)} = 2 \times \frac{\left(^{87}Sr_{(V)}/^{86}Sr_{(V)}\right) \times \sqrt{\left[(^{87}Sr + {}^{86}Sr)/(^{87}Sr \times {}^{86}Sr)\right]_{(cps)}}}{\sqrt{\text{no.cycles}}} \quad (3)$$

The CS describes the uncertainty inherent in approximating a continuous quantity, such as signal intensity, by measuring a finite number of individual events that are randomly distributed in time, such as ions arriving at the Faraday detectors. The theoretical curves for the contribution of the CS and the JN on the 2 s.e. of the $^{87}Sr/^{86}Sr$ ratio are plotted in Fig. 7 as a function of the $^{86}Sr^{+}$ intensity, along with LA-ICP-MS data obtained on the Durango apatite with 10^{11} Ω amplifiers (Buzenchi et al., 2023; 122 analyses) and 10^{13} Ω amplifiers (this study; 84 analyses). The sum of CS and JN (eq. 4), which is illustrated by the solid green curve (10^{13} Ω data) and the solid red curve (10^{11} Ω data) in Fig. 7, represents the best precision that can theoretically be achieved depending on the measured $^{86}Sr^{+}$ intensity. For 10^{11} Ω amplifiers, the (CS + JN) curve plots close to the JN curve, which highlights the major influence of the JN on the precision of measurements at low intensity beams with low-ohmic resistors. In contrast, the (CS + JN) curve plots close to the CS curve for 10^{13} Ω amplifiers.

Table 3
LA-MC-ICP-MS data for matrix apatites and apatite inclusions in zircons from the Strontian pluton. Intensities for each *m/z* (including during gas background measurements) and $^{87}Rb/^{86}Sr$ ratios are available in Supplementary material.

Sample name	Length x width of laser beam (μm)	Total Sr(V)	$^{87}Sr/^{86}Sr$	2 s.e.	2 s.e. (‰)	no. cycles
SR1 - matrix						
11ap-A	13 × 13	0.30	0.705452	0.000196	0.28	58
11ap-B	13 × 13	0.26	0.705252	0.000243	0.35	54
12ap-A	13 × 13	0.26	0.705529	0.000277	0.39	57
12ap-B	13 × 13	0.27	0.705297	0.000224	0.32	57
13ap-A	13 × 13	0.26	0.705513	0.000236	0.34	58
13ap-B	13 × 13	0.23	0.705198	0.000290	0.41	55
14ap-A	13 × 13	0.27	0.705367	0.000215	0.31	58
14ap-B	13 × 13	0.28	0.705233	0.000243	0.34	59
SR1 - inclusion						
03	16 × 6	0.19	0.704888	0.000871	1.2	8
05	7 × 7	0.07	0.705340	0.000647	0.92	6
06	35 × 3	0.31	0.706108	0.000716	1.0	6
13 A	10 × 10	0.13	0.706166	0.000990	1.4	11
SR2 - matrix						
11ap-A	9 × 9	0.23	0.705817	0.000227	0.32	58
11ap-B	9 × 9	0.22	0.706053	0.000293	0.41	58
12ap-A	9 × 9	0.22	0.706080	0.000232	0.33	58
12ap-B	9 × 9	0.24	0.705906	0.000204	0.29	56
14ap-A	9 × 9	0.25	0.705768	0.000228	0.32	57
14ap-B	9 × 9	0.22	0.705922	0.000224	0.32	56
15ap-A	9 × 9	0.25	0.706107	0.000261	0.37	58
15ap-B	9 × 9	0.23	0.705988	0.000250	0.36	57
SR2 - inclusion						
20	11 × 10	0.31	0.705831	0.000291	0.41	29
22 A	10 × 10	0.27	0.706109	0.000293	0.42	18
22B	8 × 6	0.15	0.706059	0.001194	1.7	19
SR3 - matrix						
13ap-A	12 × 12	0.29	0.705328	0.000235	0.33	58
13ap-B	12 × 12	0.28	0.704990	0.000232	0.33	59
29ap-A	12 × 12	0.30	0.705434	0.000193	0.27	57
29ap-B	12 × 12	0.28	0.705140	0.000185	0.26	58
30ap-A	12 × 12	0.30	0.705239	0.000161	0.23	57
30ap-B	12 × 12	0.29	0.705446	0.000200	0.28	58
31ap-A	12 × 12	0.31	0.705195	0.000183	0.26	58
31ap-B	12 × 12	0.31	0.705267	0.000174	0.25	58
SR3 - inclusion						
04-BRS	20 × 7	0.16	0.704601	0.000652	0.93	24
55	8 × 8	0.14	0.705097	0.000560	0.79	20
SR4 - matrix						
24ap-A	12 × 12	0.27	0.705555	0.000230	0.33	58
24ap-B	12 × 12	0.23	0.705526	0.000273	0.39	56
25ap-A	12 × 12	0.29	0.705626	0.000186	0.26	57
25ap-B	12 × 12	0.29	0.705589	0.000147	0.21	57
31ap-A	12 × 12	0.30	0.705616	0.000205	0.29	56
31ap-B	12 × 12	0.29	0.705433	0.000175	0.25	58
32ap-A	12 × 12	0.29	0.705536	0.000193	0.27	55
32ap-B	12 × 12	0.30	0.705546	0.000196	0.28	55
SR4 - inclusion						
26	5 × 5	0.10	0.705398	0.001075	1.5	8
38	25 × 4	0.26	0.705590	0.000910	1.3	9
47	12 × 12	0.27	0.705520	0.000301	0.43	22
50	12 × 10	0.24	0.705550	0.000336	0.48	25

$$CS + JN = 2 \times \sqrt{s.e.CS^2 + s.e.JN^2} \quad (4)$$

Interestingly, both 10^{11} Ω and 10^{13} Ω data of apatites analysed by LA-MC-ICP-MS follow the (CS + JN) curves for measured $^{86}Sr^+$ intensities between 0.006 V and 0.4 V, which suggests that an ultimate precision was reached for this range of intensities. In contrast, a shift of the 2 s.e. values towards higher values than those predicted by the (CS + JN) curve is observed for intensities lower than 0.006 V. This feature only concerns material ablated with the smallest laser beam size (i.e. 5 μm) that could be measured with 10^{13} Ω amplifiers. When smaller volumes of a given material are ablated, the contribution of the gas bank during the different steps of correction of the data becomes more important. This is highlighted in Fig. 7 by the dark blue to dark red colour gradient of the data points, which changes as a function of the increasing proportion of the gas blank intensity in the total intensity of the signal during ablation. When this proportion reaches 20% (red data points), a loss of precision by up to a factor of two is observed in our data.

Table 4
LA-MC-ICP-MS data for matrix apatites and apatite inclusions in zircon from the Rogart pluton. Intensities for each *m/z* (including during gas background measurements) and $^{87}Rb/^{86}Sr$ ratios are available in Supplementary material.

Sample name	Length x width of laser beam (μm)	Total Sr(V)	$^{87}Sr/^{86}Sr$	2 s.e.	2 s.e. (‰)	no. cycles
R2 - matrix						
04ap-A	12 × 12	0.31	0.706256	0.000180	0.26	56
04ap-B	12 × 12	0.30	0.706406	0.000183	0.26	58
06ap-A	12 × 12	0.30	0.706329	0.000210	0.30	58
06ap-B	12 × 12	0.32	0.706342	0.000166	0.24	58
07ap-A	12 × 12	0.30	0.706231	0.000172	0.24	58
07ap-B	12 × 12	0.30	0.706256	0.000189	0.27	57
08ap-A	12 × 12	0.30	0.706289	0.000178	0.25	59
08ap-B	12 × 12	0.30	0.706397	0.000194	0.27	58
R2 - inclusion						
61	10 × 8	0.17	0.706021	0.001039	1.5	7
63	15 × 8	0.15	0.705794	0.000418	0.59	8
65	20 × 8	0.24	0.707089	0.000641	0.91	9
RGH1 - matrix						
11ap-A	11 × 11	0.29	0.706107	0.000149	0.21	56
11ap-B	11 × 11	0.29	0.706127	0.000225	0.32	56
12ap-A	11 × 11	0.30	0.705983	0.000170	0.24	58
12ap-B	11 × 11	0.30	0.706267	0.000192	0.27	56
13ap-A	11 × 11	0.29	0.706081	0.000220	0.31	58
13ap-B	11 × 11	0.28	0.706040	0.000188	0.27	57
14ap-A	11 × 11	0.29	0.706421	0.000166	0.24	57
14ap-B	11 × 11	0.29	0.705832	0.000177	0.25	55
RGH1 - inclusion						
69	20 × 5	0.27	0.706191	0.000515	0.73	10
79	10 × 10	0.19	0.706205	0.000708	1.0	11
83	15 × 9	0.23	0.706269	0.000258	0.37	42
RT1 - matrix						
11ap-A	12 × 12	0.28	0.706158	0.000234	0.33	58
11ap-B	12 × 12	0.27	0.706241	0.000197	0.28	56
12ap-A	12 × 12	0.27	0.705923	0.000219	0.31	56
12ap-B	12 × 12	0.27	0.706141	0.000241	0.34	57
13ap-A	12 × 12	0.22	0.706576	0.000335	0.47	58
13ap-B	12 × 12	0.24	0.706209	0.000227	0.32	56
14ap-A	12 × 12	0.26	0.706113	0.000244	0.35	59
14ap-B	12 × 12	0.26	0.706218	0.000191	0.27	56
RT1 - inclusion						
91	26 × 3	0.24	0.705652	0.000798	1.1	6
92	20 × 4	0.23	0.706005	0.000466	0.66	10
100	10 × 10	0.22	0.706419	0.000352	0.50	11
03-BRS	9 × 8	0.28	0.705325	0.000916	1.3	9
05-BRS	20 × 9	0.31	0.706291	0.000367	0.52	5
06-BRS	9 × 9	0.29	0.705434	0.000750	1.1	7

Overall, the in situ analysis of small volumes of apatite standards demonstrates the importance of improving the signal-to-noise ratio when measuring small intensity ion beams currents, especially when a correction for isobaric interferences should be performed. The enhancement of the S/N provided by 10^{13} Ω amplifiers is crucial for measuring Sr isotope ratios with the highest precision. For high-REE standards (e.g., Durango apatite with REE/Sr > 0.1), an internal precision better than 2.2‰ (2 s.e.) can be achieved with a square-shaped laser ablation beam of 5 μm and a volume of ablated material of ~250 μm^3. This opens up new avenues for the analysis of minute apatite inclusions in zircon, and our new approach was applied to a selection of natural samples of Palaeozoic age in Section 4 below.

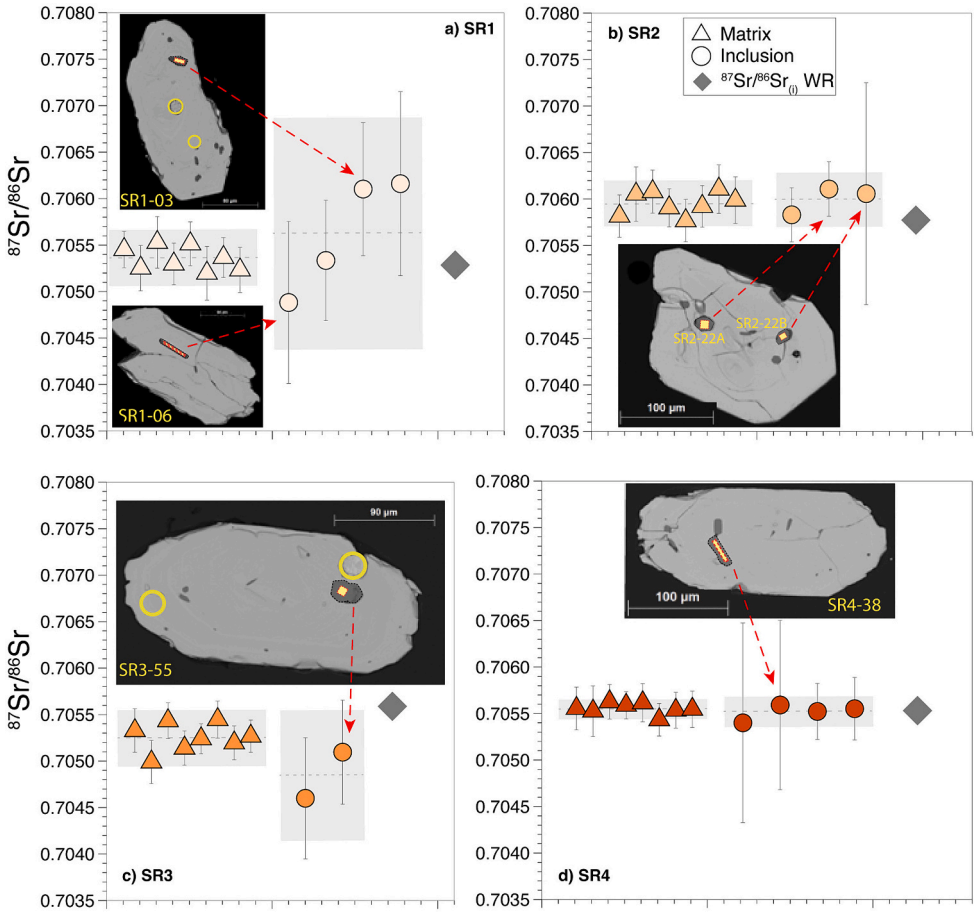

Fig. 8. LA-MC-ICP-MS Sr isotope data for matrix apatite (triangles) and apatite inclusions in zircon (circles) from the Strontian pluton. Error bars are 2 s.e. Grey dashed lines and grey fields represent the average value for each group and the associated 2 s.d., respectively. Grey diamonds are whole rock data from Fowler et al. (2008), with error bars smaller than the symbol.

4. Geological application: Analysis of matrix apatite and apatite inclusions in zircon

4.1. Geological background and methods

Matrix apatites and apatite inclusions in zircon were selected from 6 high Ba—Sr granitoids (SR1, SR3, SR4, RT1, R2, RHG1) and one high Ba—Sr appinite (SR2) from the late Caledonian (ca. 420–425 Ma) Rogart and Strontian igneous complexes from the Northern Highland Terrane in Scotland. Bulk rock chemistry, stable (O) and radiogenic (Sr and Nd) isotopes analyses were previously done by Fowler et al. (2008, 2001), while a detailed petrographic study along with in situ analyses of trace elements in titanite, zircon, apatite and apatite inclusions, O and Nd isotopes in apatite and titanite, and Hf isotopes in zircon, were more recently done by Bruand et al. (2023, 2020, 2019, 2017, 2016, 2014). These high Ba—Sr granitoids share a common source and define an array of compositions in the $\varepsilon Nd_{(i)}$ versus Sr isotopic space along the so called 'Caledonian Parental Magma Array' (CPMA; Fowler et al., 2008).

Samples from the Rogart pluton are characterised by negative $\varepsilon Nd_{(i)}$ (−2 to −5) and $^{87}Sr/^{86}Sr_i$ ratios between 0.706 and 0.709 (Fowler et al., 2001), while Strontian pluton samples have positive $\varepsilon Nd_{(i)}$ (0–1.5) and less radiogenic $^{87}Sr/^{86}Sr_{(i)}$ (0.705–0.706) (Fowler et al., 2008). Trace element compositions and Nd and O isotopes on accessory minerals evidenced that apatite and titanite record the primary composition of the whole rock (Bruand et al., 2019, 2023). Zircons containing apatite inclusions were previously analysed for U—Pb and Hf isotopes by Bruand et al. (2023), and their data indicate that most of the zircons are concordant and have more or less homogenous Hf isotope compositions (Rogart $\varepsilon Hf_{(i)} = -5.8 \pm 0.3$ (2 s.d.) and Strontian $\varepsilon Hf_{(i)} = -1.3 \pm 1.7$ (2 s.d.)). Apatite inclusions in zircon were also studied for trace elements (Bruand et al., 2014), and these samples are therefore ideal to test the new methodology developed in this contribution.

For each sample, we selected 4 apatites in the rock matrix to perform two LA-MC-ICP-MS analyses on each grain. Depending on the size and the internal structures of the grains, a square-shaped laser ablation beam size of 10 µm or 13 µm was used. The fluence was set at 6 J/cm^2 and the repetition rate at 5 Hz. Apatite inclusions in zircon were analysed with the same fluence and repetition rate, and laser ablation beams with rectangular shapes and various aspect ratios and orientations were used to analyse the largest volume of apatite inclusions exposed at the surface.

During ablation, the intensities on *m/z* 83.5 and 86.5 were monitored to identify shifts in the signal that might indicate a contribution from the host zircon. Zircon contains high amounts of Hf, Yb and Er, and very low amounts of Sr (Grimes et al., 2007). In the same way as for Er and Yb, Hf can form doubly-charged interferences on *m/z* 83.5 and 86.5 (Table 1), so when an important drop of Sr intensities was observed simultaneously with an increase of intensities on *m/z* 83.5 and 86.5, the ablation was aborted and the cycles associated to zircon ablation were excluded from the calculation of the final $^{87}Sr/^{86}Sr$ ratio. This explains why a lower number of cycles (down to 6) was integrated for apatite inclusion analysis in Table 3. Low intensities (i.e. <0.2 mV) of ^{87}Rb may remain after isobaric interference corrections; however, since the contribution of the radiogenic decay of ^{87}Rb in the calculation of initial $^{87}Sr/^{86}Sr$ ratios was <100 ppm, which is well within the uncertainty of individual analyses, only measured $^{87}Sr/^{86}Sr$ were considered in the

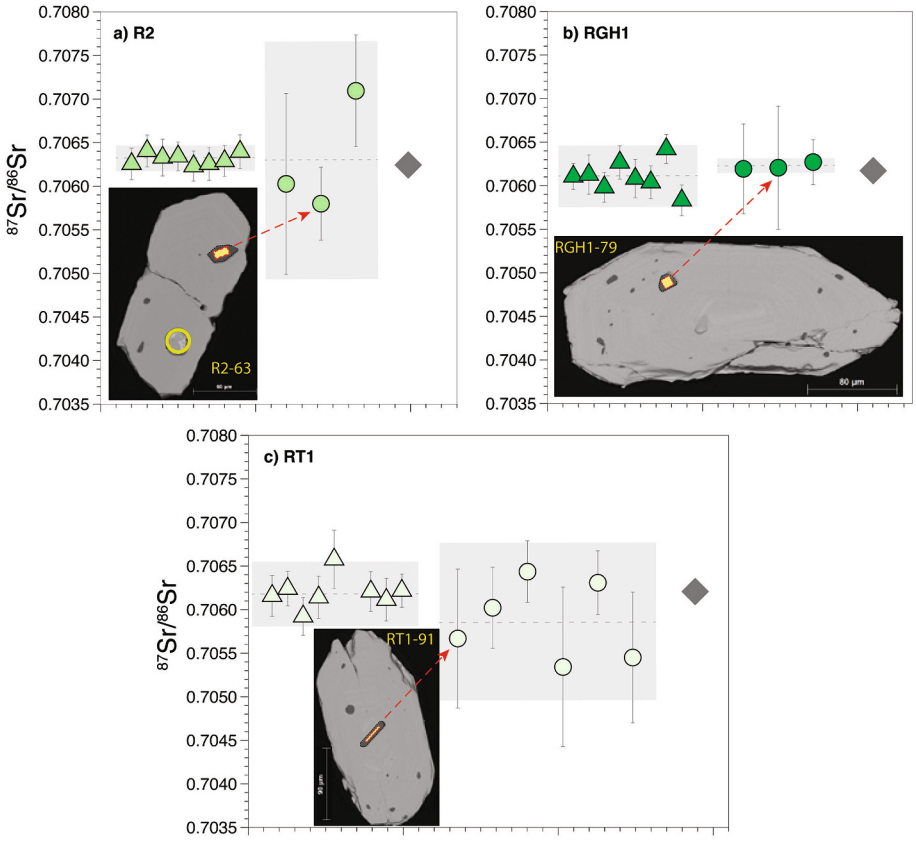

Fig. 9. LA-MC-ICP-MS Sr isotope data for matrix apatite (triangles) and apatite inclusions in zircon (circles) from the Rogart pluton. Error bars are 2 s.e. Grey dashed lines and grey fields represent the average value for each group and the associated 2 s.d., respectively. Grey diamonds are whole rock data from Fowler et al. (2001), with error bars smaller than the symbol.

following sections.

4.2. Comparison between laser ablation and whole rock data

A total of 56 LA-MC-ICP-MS analyses were performed on matrix apatites, along with 26 measurements of apatite inclusions in zircon (Table 3 and Table 4). All raw data were corrected with the *Method 2* data reduction procedure of Buzenchi et al. (2023) (See Section 2.3). The accuracy and long-term reproducibility of the measurements were assessed by performing repeated analyses of the Durango apatite with a square-shaped 13 μm laser beam (Supplementary material). An average $^{87}Sr/^{86}Sr$ ratio of 0.706413 ± 0.000347 (2 s.d.; $n = 20$) was obtained, which is within error of the published values of Yang et al. (2014b) and Buzenchi et al. (2023). Overall, the internal precision (2 s.e) of matrix apatites analyses is better than 0.47‰ (average precision for 56 analyses = 0.30 ‰), and it is better than 1.7 ‰ for apatite inclusions (average precision for 26 analyses = 0.91 ‰).

The $^{87}Sr/^{86}Sr$ ratios measured in matrix apatites and apatites inclusions are plotted in Figs. 8 and 9, along with the ID-TIMS whole rock (WR) data of Fowler et al. (2008, 2001) Backscattered electrons (BSE) images of selected zircons with apatite inclusions are shown as insets in Figs. 8 and 9. All BSE images of zircons hosting apatite inclusions, along with cathodoluminescence (CL) images of the matrix apatites analysed are provided as Supplementary material.

Matrix apatites from Strontian samples (SR1, SR2, SR3 and SR4) have average $^{87}Sr/^{86}Sr$ ratios ranging from 0.705255 ± 0.000304 to 0.705955 ± 0.000247. For samples SR1, SR2 and SR4, average $^{87}Sr/^{86}Sr$ ratios of matrix apatites are within error of the WR ratios (Figs. 8a, b, d). In contrast, the average $^{87}Sr/^{86}Sr$ ratios of matrix apatites in sample SR3 is slightly lower than the WR ratio (Fig. 8c). For all samples, the $^{87}Sr/^{86}Sr$ ratios measured in apatite inclusions are within error of the average ratios of the matrix apatites, with sample SR1 having the largest range of Sr isotope variation observed in apatite inclusions.

Matrix apatites from Rogart samples (R2, RGH1 and RT1) have average $^{87}Sr/^{86}Sr$ ratios ranging from 0.706107 ± 0.000355 ($n = 8$) to 0.706313 ± 0.000132 ($n = 8$; 2 s.d.). All average $^{87}Sr/^{86}Sr$ ratios of matrix apatites are within error of the WR ratios (Fig. 9). $^{87}Sr/^{86}Sr$ ratios measured in apatite inclusions are within error of the average ratios of matrix apatites, with sample R2 having the largest range of Sr isotope variation observed in apatite inclusions.

4.3. Magma genesis and evolution through the accessory minerals record

Our samples belong to two localities with distinct isotopic signatures, ranging from relatively depleted (Strontian) to relatively enriched (Rogart). In the Nd—Sr isotope space, they plot along the "Caledonian Parental Magma Array" (CPMA; Fowler et al. (2008)) that defines evolving compositions of the mafic source of plutonic rocks in the Northern Highland Terrane. In Fig. 10, the $^{87}Sr/^{86}Sr$ average data of matrix apatite and apatite inclusions in zircon are plotted against the εNd data of Bruand et al. (2023), which was obtained from the in situ analysis of matrix apatites; except for sample SR1, for which apatite data are not available. Since εNd values in apatite are within error of εNd values in titanite in the samples investigated (Bruand et al., 2023), the titanite εNd data of sample SR1 could be plotted in Fig. 10. The field of compositions of whole rock values of the Strontian and Rogart plutons (Fowler et al., 2008) is also plotted in this figure.

For the Strontian pluton, the in situ data define a decreasing trend in the Nd—Sr isotopic space, from sample SR3 (most depleted) to sample SR2 (most enriched). (Fig. 10). For the Rogart, all data can be considered as similar within error, and samples define no obvious trend. On the basis of the whole rock isotope data, Fowler et al. (2008) suggested that

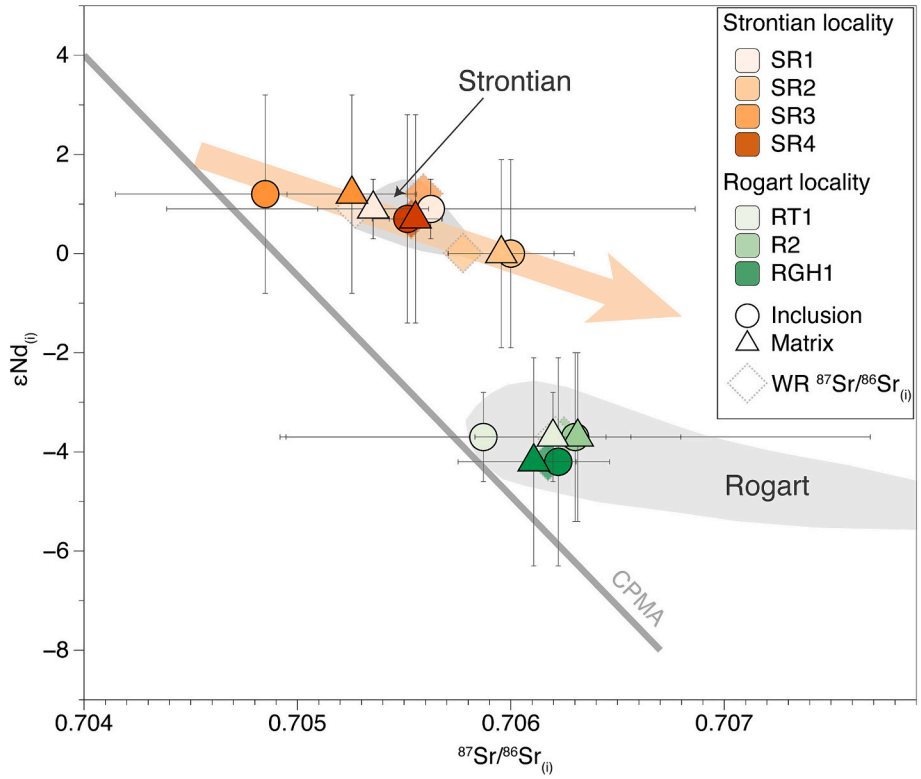

Fig. 10. $\varepsilon Nd_{(i)}$ vs $^{87}Sr/^{86}Sr_{(i)}$ plot for Caledonian high Ba—Sr granitoids from Fowler et al. (2008, 2001) showing the fields of compositions for Rogart and Strontian plutons from the Northern Highland Terrane (grey fields) and the average results from matrix and apatite inclusions in zircons. εNd data are from Bruand et al. (2023) (error bars are 2 s.d.). Diamonds are WR $\varepsilon Nd_{(i)}$ and $^{87}Sr/^{86}Sr_{(i)}$ compositions from Fowler et al. (2008, 2001).

both plutons have been affected by the assimilation, in various proportions, of Moine metasediments into their CPMA magmatic source. While our data suggest a rather homogenous composition of the Rogart pluton, at least from the samples investigated (Figs. 8 and 9), the combination of in situ Sr and Nd isotope data confirms that the isotopic composition of the Strontian pluton extends from the CPMA towards a more enriched end-member. The most mafic magmas in the Strontian, such as appinites, may have formed from a mantle source enriched in K, Ba, Sr and LREE, through a contamination by fluids and/or melts derived from subducted pelagic sediments and carbonates (Fowler et al., 2008). This is consistent with the enriched Sr isotope signature of sample SR2, which is the most mafic sample that we analysed in the Strontian pluton.

In summary, our data confirm that apatite has a great potential to faithfully retain the primary signature of its source magma. The LA-MC-ICP-MS approach that we developed here may be further used to analyse samples that were affected by secondary processes, and for which the whole rock original geochemical signature is lost.

5. Conclusions

Repeated analyses of Sr isotopes in apatite show that 10^{13} Ω current amplifiers can improve both the internal precision and the external reproducibility LA-MC-ICP-MS analyses by ca. 4 times. The approach developed in this study enables the analysis of high-REE apatite (e.g., Durango) with an average precision of 2.2‰ for a volume of ablated material of ~250 μm^3. For an ablated volume of ~1500 μm^3, the precision becomes better than 1.7‰ for this standard, and it remains better than 2.2‰ for low-Sr apatites such as Ipirá with ~250 ppm Sr. This study further demonstrates that when using 10^{13} Ω amplifiers, the internal precision of $^{87}Sr/^{86}Sr$ ratios is mostly governed by the counting statistics, and to a lesser degree by the instrumental noise. At very low signal intensities (typically <0.006 V) the precision obtained may become worse than the predicted precision because of the increasing contribution of the background correction in the total signal.

The application of our approach to natural samples from the Northern Highland Terrane (Scotland) shows that $^{87}Sr/^{86}Sr$ ratios can be measured routinely with an average precision of 0.3 ‰ and 0.9 ‰ on matrix apatite and apatite inclusions in zircon, respectively. For the seven samples investigated, our data shows a good consistency between $^{87}Sr/^{86}Sr$ ratios in the whole rock, in matrix apatites, and in apatite inclusions in zircon. These results confirm the ability of apatite to record the geochemical signature of its parent magma (Bruand et al., 2016; Dhuime et al., 2014; Emo et al., 2018; Gillespie et al., 2021a). Overall, the analysis of Sr isotopes in apatite inclusions in both magmatic and detrital zircons with a large range of crystallisation ages and provenances has a great potential to expand our understanding of the formation and the evolution of the continental crust since Earth's formation.

CRediT authorship contribution statement

Anda Buzenchi: Visualization, Validation, Methodology, Investigation, Formal analysis, Data curation, Conceptualization, Writing – review & editing, Writing – original draft. **Hugo Moreira:** Visualization, Resources, Methodology, Conceptualization, Writing – review & editing. **Emilie Bruand:** Resources, Formal analysis, Conceptualization, Writing – review & editing. **Olivier Bruguier:** Methodology, Formal analysis, Writing – review & editing. **Bruno Dhuime:** Validation, Supervision, Resources, Project administration, Methodology, Funding acquisition, Formal analysis, Conceptualization, Writing – review & editing, Writing – original draft.

Declaration of competing interest

The authors declare that they have no known competing financial

interests or personal relationships that could have appeared to influence the work reported in this paper.

Data availability

The data is available in the supplementary material.

Acknowledgments

This project was funded by the European Research Council under the European Union's Horizon 2020 research and innovation program (No. 817934). We thank Sonja Aulbach for the editorial handling, as well as the two anonymous reviewers for their constructive comments and suggestions.

Appendix A. Supplementary data

Supplementary data to this article can be found online at https://doi.org/10.1016/j.chemgeo.2024.122306.

References

Alba, M., Tanner De Olveira, F., Paolo Sighinolfi, G., 1983. Geochemistry of Precambrian phosphate-carbonate intrusives from Bahia (Brazil). Geochem. J. 17, 277–287. https://doi.org/10.2343/geochemj.17.277.

Bruand, E., Storey, C., Fowler, M., 2014. Accessory Mineral Chemistry of High Ba–Sr Granites from Northern Scotland: Constraints on Petrogenesis and Records of Whole-rock Signature. J. Petrol. 55, 1619–1651. https://doi.org/10.1093/petrology/egu037.

Bruand, E., Storey, C., Fowler, M., 2016. An apatite for progress: Inclusions in zircon and titanite constrain petrogenesis and provenance. Geology 44, 91–94. https://doi.org/10.1130/G37301.1.

Bruand, E., Fowler, M., Storey, C., Darling, J., 2017. Apatite trace element and isotope applications to petrogenesis and provenance. Am. Mineral. 102, 75–84. https://doi.org/10.2138/am-2017-5744.

Bruand, E., Storey, C., Fowler, M., Heilimo, E., 2019. Oxygen isotopes in titanite and apatite, and their potential for crustal evolution research. Geochim. Cosmochim. Acta 255, 144–162. https://doi.org/10.1016/j.gca.2019.04.002.

Bruand, E., Fowler, M., Storey, C., Laurent, O., Antoine, C., Guitreau, M., Heilimo, E., Nebel, O., 2020. Accessory mineral constraints on crustal evolution: elemental fingerprints for magma discrimination. Geochem. Persp. Let. 7–12 https://doi.org/10.7185/geochemlet.2006.

Bruand, E., Storey, C., Fowler, M., Dhuime, B., Doucelance, R., 2023. Mineral-whole rock isotope fidelity? A comparative study of Hf-Nd-O from high Ba-Sr granitoids. Chem. Geol. 624, 121425 https://doi.org/10.1016/j.chemgeo.2023.121425.

Buzenchi, A., Moreira, H., Bruguier, O., Bosch, D., Dhuime, B., 2023. High-spatial resolution (10–50 μm) analysis of Sr isotopes in rock-forming apatite by LA-MC-ICP-MS. J. Anal. At. Spectrom. https://doi.org/10.1039/D3JA00177F.

Caton, S.A., Smit, M.A., Emo, R.B., Musiyachenko, K.A., Kielman-Schmitt, M., Kooijman, E., Scherstén, A., Halla, J., Bleeker, W., Hoffmann, J.E., Pandey, O.P., Ravindran, A., Maltese, A., Mezger, K., 2022. Evolution of the sources of TTG and associated rocks during the Archean from in-situ 87Sr/86Sr isotope analysis of apatite by LA-MC-ICPMS. Lithos 428–429, 106830. https://doi.org/10.1016/j.lithos.2022.106830.

Chew, D.M., Sylvester, P.J., Tubrett, M.N., 2011. U–Pb and Th–Pb dating of apatite by LA-ICPMS. Chem. Geol. 280, 200–216. https://doi.org/10.1016/j.chemgeo.2010.11.010.

Craig, G., Hu, Z., Zhang, A., Lloyd, N.S., Bouman, C., Schwieters, J., 2017. Thermo Scientific Neptune Plus MC-ICP-MS with 1013 Ω Amplifier Technology.

Craig, G., Managh, A.J., Stremtan, C., Lloyd, N.S., Horstwood, M.S.A., 2018. Doubling Sensitivity in Multicollector ICPMS using High-Efficiency, Rapid Response Laser Ablation Technology. Anal. Chem. 90, 11564–11571. https://doi.org/10.1021/acs.analchem.8b02896.

Craig, G., Hu, Z., Zhang, A., Lloyd, N.S., Bouman, C., Schwieters, J., 2019. Dynamic Time Correction for High Precision Isotope Ratio Measurements.

Creech, J.B., Schaefer, B.F., Turner, S.P., 2020. Application of 10 ^{13} Ω Amplifiers in Low-Signal Plasma-Source Isotope Ratio Measurements by MC-ICP-MS: a Case Study with Pt Isotopes. Geostand. Geoanal. Res. 44, 223–229. https://doi.org/10.1111/ggr.12310.

Dhuime, B., Hawkesworth, C.J., Cawood, P.A., Storey, C.D., 2012. A Change in the Geodynamics of Continental Growth 3 billion years Ago. Science 335, 1334–1336. https://doi.org/10.1126/science.1216066.

Dhuime, B., Lewis, J., Bruand, E., Hawkesworth, C., 2014. New insights into crustal evolution studies from Sr isotopes. In: EGU General Assembly Conference Abstracts, EGU General Assembly Conference Abstracts, p. 4173.

Emo, R.B., Smit, M.A., Schmitt, M., Kooijman, E., Scherer, E.E., Sprung, P., Bleeker, W., Mezger, K., 2018. Evidence for evolved Hadean crust from Sr isotopes in apatite within Eoarchean zircon from the Acasta Gneiss complex. Geochim. Cosmochim. Acta 235, 450–462. https://doi.org/10.1016/j.gca.2018.05.028.

Fowler, M., Rollinson, H., 2012. Phanerozoic sanukitoids from Caledonian Scotland: implications for Archean subduction. Geology 40, 1079–1082.

Fowler, M., Henney, P., Darbyshire, D.F., Greenwood, P., 2001. Petrogenesis of high Ba–Sr granites: the Rogart pluton, Sutherland. J. Geol. Soc. Lond. 158, 521–534.

Fowler, M., Kocks, H., Darbyshire, D., Greenwood, P., 2008. Petrogenesis of high Ba–Sr plutons from the northern highlands Terrane of the British Caledonian Province. Lithos 105, 129–148.

Gillespie, J., Kinny, P.D., Kirkland, C.L., Martin, L., Nemchin, A.A., Cavosie, A.J., Hasterok, D., 2021a. Isotopic modelling of Archean crustal evolution from comagmatic zircon–apatite pairs. Earth Planet. Sci. Lett. 575, 117194 https://doi.org/10.1016/j.epsl.2021.117194.

Gillespie, J., Nemchin, A.A., Kinny, P.D., Martin, L., Aleshin, M., Roberts, M.P., Ireland, T.R., Whitehouse, M.J., Jeon, H., Cavosie, A.J., Kirkland, C.L., 2021b. Strontium isotope analysis of apatite via SIMS. Chem. Geol. 559, 119979 https://doi.org/10.1016/j.chemgeo.2020.119979.

Grimes, C.B., John, B.E., Kelemen, P.B., Mazdab, F.K., Wooden, J.L., Cheadle, M.J., Hanghøj, K., Schwartz, J.J., 2007. Trace element chemistry of zircons from oceanic crust: a method for distinguishing detrital zircon provenance. Geol 35, 643. https://doi.org/10.1130/G23603A.1.

Horstwood, M.S.A., Evans, J.A., Montgomery, J., 2008. Determination of Sr isotopes in calcium phosphates using laser ablation inductively coupled plasma mass spectrometry and their application to archaeological tooth enamel. Geochim. Cosmochim. Acta 72, 5659–5674. https://doi.org/10.1016/j.gca.2008.08.016.

John, S.G., Adkins, J.F., 2010. Analysis of dissolved iron isotopes in seawater. Mar. Chem. 119, 65–76. https://doi.org/10.1016/j.marchem.2010.01.001.

Kemp, A.I.S., Wilde, S.A., Hawkesworth, C.J., Coath, C.D., Nemchin, A., Pidgeon, R.T., Vervoort, J.D., DuFrane, S.A., 2010. Hadean crustal evolution revisited: New constraints from Pb–Hf isotope systematics of the Jack Hills zircons. Earth Planet. Sci. Lett. 296, 45–56. https://doi.org/10.1016/j.epsl.2010.04.043.

Kimura, J.-I., Chang, Q., Kanazawa, N., Sasaki, S., Vaglarov, B.S., 2016. High-precision in situ analysis of Pb isotopes in glasses using 10 ^{13} Ω resistor high gain amplifiers with ultraviolet femtosecond laser ablation multiple Faraday collector inductively coupled plasma mass spectrometry. J. Anal. At. Spectrom. 31, 790–800. https://doi.org/10.1039/C5JA00374A.

Klaver, M., Smeets, R.J., Koornneef, J.M., Davies, G.R., Vroon, P.Z., 2016. Pb isotope analysis of ng size samples by TIMS equipped with a 10 13 Ω resistor using a 207 Pb–204 Pb double spike. J. Anal. At. Spectrom. 31, 171–178.

Koornneef, J.M., Bouman, C., Schwieters, J.B., Davies, G.R., 2014. Measurement of small ion beams by thermal ionisation mass spectrometry using new 1013Ohm resistors. Anal. Chim. Acta 819, 49–55. https://doi.org/10.1016/j.aca.2014.02.007.

Lana, C., Gonçalves, G.O., Mazoz, A., Buick, I., Kamo, S., Scholz, R., Wang, H., Moreira, H., Babinski, M., Queiroga, G., 2022. Assessing the U-Pb, Sm-Nd and Sr-Sr Isotopic Compositions of the Sumé Apatite as a Reference Material for LA-ICP-MS Analysis. Geostand. Geoanal. Res. 46, 71–95. https://doi.org/10.1111/ggr.12413.

Lloyd, N.S., Sadekov, A.Yu., Misra, S., 2018. Application of 10 ^{13} ohm Faraday cup current amplifiers for boron isotopic analyses by solution mode and laser ablation multicollector inductively coupled plasma mass spectrometry. Rapid. Comm. Mass Spectromet. 32, 9–18. https://doi.org/10.1002/rcm.8009.

Lugli, F., Weber, M., Giovanardi, T., Arrighi, S., Bortolini, E., Figus, C., Marciani, G., Oxilia, G., Romandini, M., Silvestrini, S., Jochum, K.P., Benazzi, S., Cipriani, A., 2020. Fast offline data reduction of laser ablation MC-ICP-MS Sr isotope measurements via an interactive Excel-based spreadsheet 'SrDR'. J. Anal. At. Spectrom. 35, 852–862. https://doi.org/10.1039/C9JA00424F.

Makishima, A., Nakamura, E., 2010. Precise isotopic determination of Hf and Pb at sub-nano gram levels by MC-ICP-MS employing a newly designed sample cone and a pre-amplifier with a 10 12 ohm register. J. Anal. At. Spectrom. 25, 1712–1716.

Makishima, A., Nakamura, E., 2012. High-resolution MC-ICPMS employing amplifiers with a 10 12 ohm resistor for bulk sulfur determination in biological and geological samples. J. Anal. At. Spectrom. 27, 891–895.

Müller, W., Anczkiewicz, R., 2016. Accuracy of laser-ablation (LA)-MC-ICPMS Sr isotope analysis of (bio)apatite – a problem reassessed. J. Anal. At. Spectrom. 31, 259–269. https://doi.org/10.1039/C5JA00311C.

Pettke, T., Oberli, F., Audétat, A., Wiechert, U., Harris, C.R., Heinrich, C.A., 2011. Quantification of transient signals in multiple collector inductively coupled plasma mass spectrometry: accurate lead isotope ratio determination by laser ablation of individual fluid inclusions. J. Anal. At. Spectrom. 26, 475–492. https://doi.org/10.1039/C0JA00140F.

Ramos, F.C., Wolff, J.A., Tollstrup, D.L., 2004. Measuring 87Sr/86Sr variations in minerals and groundmass from basalts using LA-MC-ICPMS. Chem. Geol. 211, 135–158. https://doi.org/10.1016/j.chemgeo.2004.06.025.

Ravindran, A., Mezger, K., Balakrishnan, S., Kooijman, E., Schmitt, M., Berndt, J., 2020. Initial 87Sr/86Sr as a sensitive tracer of Archaean crust-mantle evolution: Constraints from igneous and sedimentary rocks in the western Dharwar Craton, India. Precambrian Res. 337, 105523 https://doi.org/10.1016/j.precamres.2019.105523.

Schulz, T., Münker, C., Peters, S.T.M., 2013. P-Process 180W anomalies in iron meteorites: Nucleosynthetic versus non-nucleosynthetic origins. Earth Planet. Sci. Lett. 362, 246–257. https://doi.org/10.1016/j.epsl.2012.11.009.

Thirlwall, M.F., 1991. Long term reproducibility of multicollector Sr and Nd isotope ratio analysis. Chem. Geol.: Isot. Gesoci. sec. 94, 85–104. https://doi.org/10.1016/0168-9622(91)90002-E.

Thomson, S.N., Gehrels, G.E., Ruiz, J., Buchwaldt, R., 2012. Routine low-damage apatite U-Pb dating using laser ablation–multicollector–ICPMS. Geochem. Geophys. Geosyst. 13.

Valley, J.W., Kinny, P.D., Schulze, D.J., Spicuzza, M.J., 1998. Zircon megacrysts from kimberlite: oxygen isotope variability among mantle melts. Contrib. Mineral. Petrol. 133, 1–11.

Wieser, M.E., Schwieters, J.B., 2005. The development of multiple collector mass spectrometry for isotope ratio measurements. Int. J. Mass Spectrom. 242, 97–115. https://doi.org/10.1016/j.ijms.2004.11.029.

Yamamoto, K., Asanuma, H., Takahashi, H., Hirata, T., 2021. *In situ* isotopic analysis of uranium using a new data acquisition protocol for 10 ^{13} ohm Faraday amplifiers. J. Anal. At. Spectrom. 36, 668–675. https://doi.org/10.1039/D0JA00498G.

Yang, Y.-H., Wu, F.-Y., Xie, L.-W., Chu, Z.-Y., Yang, J.-H., 2014a. Re-evaluation of interferences of doubly charged ions of heavy rare earth elements on Sr isotopic analysis using multi-collector inductively coupled plasma mass spectrometry. Spectrochim. Acta B At. Spectrosc. 97, 118–123. https://doi.org/10.1016/j.sab.2014.05.006.

Yang, Y.-H., Wu, F.-Y., Yang, J.-H., Chew, D.M., Xie, L.-W., Chu, Z.-Y., Zhang, Y.-B., Huang, C., 2014b. Sr and Nd isotopic compositions of apatite reference materials used in U–Th–Pb geochronology. Chem. Geol. 385, 35–55. https://doi.org/10.1016/j.chemgeo.2014.07.012.